Journal of Science: Advanced Materials and Devices 10 (2025) 100847

Contents lists available at ScienceDirect

Journal of Science: Advanced Materials and Devices

journal homepage: www.elsevier.com/locate/jsamd

Research Article

Design, characterization, and electromagnetic performance of a flexible wideband RF antenna using composite materials

Saïd Douhi [a,b], Salesabil Labihi [a,b], Adil Eddiai [a,**], Soufian Lakrit [c], Mounir El Achaby [d], Ahmed Jamal Abdullah Al-Gburi [e,*]

[a] Laboratory of Physics of Condensed Matter (LPMC), Faculty of Sciences Ben M'Sick, Hassan II University of Casablanca, Sidi Othman, B.P 7955, Casablanca, Morocco
[b] REMTEX Laboratory, Higher School of Textile and Clothing Industries (ESITH), Casablanca, Morocco
[c] Mathematics and Information Systems Laboratory, EST of Nador, Mohammed First University, Oujda, Morocco
[d] Materials Science and Nanoengineering Department (MSN), Mohammed VI Polytechnic University (UM6P), Benguerir, Morocco
[e] Center for Telecommunication Research & Innovation (CeTRI), Fakulti Teknologi Dan Kejuruteraan Elektronik Dan Komputer (FTKEK), Jalan Hang Tuah Jaya, Durian Tunggal, 76100, Melaka, Malaysia

ARTICLE INFO

Keywords:
Flexible antennas
Specific absorption rate (SAR)
Dielectric properties
X-ray diffraction (XRD)
Radiation efficiency
Antenna testing
Wearable technologies
Smart composite

ABSTRACT

Traditional microwave and microelectronic technologies typically use metal components for high efficiency, but their rigidity and susceptibility to corrosion limit their suitability for wearable applications. To meet the demand for flexible, high-performance materials in wearable communication systems, this study investigates the use of Poly (vinylidene fluoride-co-hexafluoropropylene) (PVDF-HFP) combined with calcium- and zirconium-doped barium titanate (BCZT) as a novel substrate for microwave applications. A flexible wideband antenna was developed using a PVDF-HFP/BCZT composite, with BCZT particles enhancing the composite's thermal stability, crystallinity, and dielectric performance. Conductive fabric was employed for the antenna's radiating elements, supporting both flexibility and user comfort. The antenna was fabricated via laser cutting and tested in free space and on a human body model, achieving a resonant frequency of 5.94 GHz, a return loss of −48.32 dB, and a wide bandwidth of 5.10–6.40 GHz, with VSWR below 2 and a radiation efficiency of 60%. Specific absorption rate (SAR) testing with a multilayer human tissue model yielded values of 1.22 W/kg (1g) and 0.366 W/kg (10g), in compliance with international safety standards. Experimental results closely aligned with simulations, demonstrating the potential of PVDF-HFP/BCZT-based antennas as eco-friendly, high-performance solutions for wearable technologies, achieving an effective balance between flexibility and efficiency.

1. Introduction

Radiofrequency communication technology is now essential in modern life, increasing the demand for compact, lightweight, and durable antennas that enable fast and secure data transmission in devices [1–4]. Antennas convert electronic signals into electromagnetic waves that travel through free space and are essential components in terminal base stations and portable communication devices [5–7]. They are also widely used in applications such as wireless sensing, the Internet of Things (IoT), microwave imaging for cancer diagnostics, and monitoring structural integrity [8–11].

Introduced in the 1970s, microstrip antennas have gained popularity due to their high performance, compact size, ease of fabrication, and durability [12]. These antennas typically consist of a ground plane, a dielectric substrate, and a radiating patch [13]. Common substrates such as FR-4 ($\varepsilon_r = 4.4$) and RT-Duroid ($\varepsilon_r = 2.2$) play an essential role in defining antenna characteristics [14]. The dielectric constant of the substrate is particularly important in determining the antenna's size, with higher constants allowing for further miniaturization. However, this also introduces the challenge of dielectric loss, which can attenuate signals and reduce efficiency. Thus, selecting materials with high dielectric constants and low losses is essential for effective transmission [15,16]. High-dielectric-constant (high-k) materials are particularly interesting in energy harvesting and microwave communication systems [17,18]. Different strategies have been used to achieve high-k composites, such as adding conductive fillers like carbon nanotubes, graphene

* Corresponding author.
** Corresponding author.
E-mail addresses: adil.eddiai@gmail.com (A. Eddiai), ahmedjamal@ieee.org, engahmed_jamall@yahoo.com (A.J.A. Al-Gburi).

https://doi.org/10.1016/j.jsamd.2024.100847
Received 18 November 2024; Received in revised form 28 December 2024; Accepted 30 December 2024
Available online 31 December 2024

[19,20], metals, and ferroelectric ceramics like $BaTiO_3$ (BT) [21,22], $SrTiO_3$, TiO_2 [23,24], and Ba1-xSrxTiO₃ [25,26]. However, these fillers often lead to increased dielectric loss at higher frequencies, limiting their effectiveness. To address this, polymer/ceramic composites present a promising alternative, merging the adaptability of polymers with the high dielectric characteristics of ceramics, making them ideal for wearable applications.

Flexible polymer-based materials and textiles have gained increasing attention in developing stretchable, low-profile antennas for wearable electronics [27–32]. Polymer/ceramic composites, consisting of a polymer base combined with ceramic particles, are particularly valuable in wireless radio communications. These composites provide improved mechanical flexibility, customized permittivity, controlled heat resistance, and reduced energy dissipation. Notably, Poly(vinylidene fluoride) (PVDF) and its copolymers are distinguished by their superior mechanical flexibility and advantageous dielectric properties [33,34]. Similarly, ceramics such as Barium Calcium Zirconate Titanate (BCZT) are prized for their elevated dielectric constants and minimal energy dissipation, which makes them ideal for efficient energy storage and signal transmission [35].

Numerous studies have explored various substrate materials to optimize antenna performance across different applications. For instance, Ref. [36] explores the use of (1-x)$LiWVO_6$-xK_2MoO_4 (LWVO-KMO) composite ceramics in microstrip patch antennas. This study achieved a central frequency of 6.58 GHz, a bandwidth of 170 MHz, and an efficiency of 89.5%. Similarly, reference [37] focuses on PVDF/$BaFe_{11.7}Al_{0.3}O_{19}$ (HF) composites, evaluating various PVDF concentrations. The 10% PVDF composite demonstrated optimized performance at 2.45 GHz, significantly improving the antenna's gain and efficiency. For wearable technology, reference [38], utilized a PDMS-$BaTiO_3$-PTFE composite substrate for an ultra-wideband antenna. This antenna exhibited flexible characteristics and a broad frequency range (2–13 GHz), with a relative bandwidth of 146.7%. In Ref. [39], a micro-crosslinked polyimide (PI) nanocomposite with a dielectric constant of 2.40 and a low loss tangent (0.0017) is used for microwave antennas, showing reduced signal loss ($S_{11} = -10.874$ dB) and improved magnetic fields at 3.0 GHz. Finally, reference [40], investigates a bilayer Fe_2O_3/PDMS and PTFE/PDMS composite for RFID applications, achieving high reflection loss (up to 47.98 dB) and improving tag recovery rate to 87.57%, enhancing interference reduction and electromagnetic wave absorption.

This work presents a novel flexible and low-profile wideband antenna designed for wearable technologies, utilizing a composite substrate of PVDF-HFP and BCZT. The PVDF-HFP matrix offers mechanical flexibility, while BCZT significantly improves the dielectric properties, marking the first application of this composite in wearable antennas. Conductive textiles are employed for the antenna's feeding and radiating elements, resulting in a lightweight, metal-free design ideal for portable telecommunication devices. The antenna features a simple offset rectangular patch with three slots for performance optimization and a circular parasitic element on the opposite side of the substrate, excited by a microstrip line to maintain a compact profile. Performance evaluations, conducted using ANSYS HFSS and validated with CST Microwave Studio (MWS) 2019®, revealed an operational frequency of 5.94 GHz, a return loss of −48.32 dB, an impedance bandwidth ranging from 5.10 GHz to 6.40 GHz, and a radiation efficiency of 60%. Specific absorption rate (SAR) measurements confirm adherence to international safety standards, ensuring the antenna's suitability for wearable devices. This research demonstrates the potential of PVDF-HFP/BCZT composite antennas as flexible, high-performance, and environmentally sustainable solutions for next-generation wireless body area networks and wearable devices.

2. Materials and methods

2.1. Fabrication and characterization of composite films

In this work, N, N-dimethylformamide (DMF), and Poly (vinylidene fluoride-co-hexafluoropropylene) (PVDF-HFP), obtained from Sigma Aldrich, served as the main materials. PVDF-HFP possesses a density of 1.77 g/cm^3, a melting point range of 140 °C–144 °C, and a molar mass of 64.03 g/mol. The active filler, Barium Calcium Zirconate Titanate (BCZT), was provided by the Ceramic Materials and Mathematics Laboratory (CERAMATHS) at the Polytechnic University Hauts-de-France. The PVDF-HFP/BCZT composite films were prepared through the solvent-casting technique, as depicted in Fig. 1. To fabricate the films, 2.0 g of PVDF-HFP pellets were dissolved in DMF at 70 °C for 2 h to ensure full dissolution. Subsequently, BCZT was dispersed in the DMF solution through ultrasonic agitation over 2 h, with weight ratios of 10% and 15% (wt%). For the 10% composite, 0.2 g of BCZT was incorporated into 1.8 g of PVDF-HFP, and for the 15% composite, 0.3 g of BCZT was combined with 1.7 g of PVDF-HFP. A reference sample was also prepared using 2.0 g of PVDF-HFP without BCZT. After ultrasonic dispersion, the BCZT/DMF mixture was blended with the PVDF-HFP solution, followed by a 30-min stirring at 70 °C. This step was succeeded by an additional 2 h of ultrasonication to ensure uniform distribution of BCZT particles throughout the polymer matrix. The final mixtures were cast into even films using the Doctor Blade method, ensuring a consistent thickness and a smooth surface. These composite films designated BCZT X (where X = 10 or 15, according to the BCZT weight ratio), were optimized for a balance between mechanical flexibility and functional properties. BCZT content was capped at 15% to retain flexibility while enhancing energy harvesting efficiency. The preparation method for PVDF-HFP/BCZT composites aligns with the process detailed in our previous study [41].

2.2. Testing and characterization of composite substrate properties

2.2.1. X-ray diffraction (XRD)

X-ray diffraction (XRD) patterns for all samples were measured using a Bruker D8 diffractometer with Cu Kα radiation (wavelength = 1.54184 Å). Data were collected in the 2θ range of 10°–70° for BCZT powders and 5°–80° for PVDF-HFP/BCZT composites. The grain size of the BCZT powders was estimated using Scherrer's equation:

$$D = \frac{0.9 \times \lambda}{\beta \times \cos\theta} \quad (1)$$

In this equation, D represents the average grain size, λ is the X-ray wavelength (1.5405 Å for Cu Kα), β is the full width at half maximum (FWHM) in radians, and θ is the Bragg angle in degrees. The shape factor, k is conventionally taken as 0.9 for typical materials.

Fig. 2 illustrates the X-ray diffraction (XRD) patterns for pure PVDF-HFP films and PVDF-HFP/BCZT composites. In the pure PVDF-HFP film, diffraction peaks are observed at 2θ = 15.60°, 17.22°, and 24.36°, corresponding to the (020), (110), and (021) crystalline planes of the α-phase, respectively. The addition of BCZT particles into the PVDF-HFP matrix results in a significant reduction in the intensity of the peaks associated with the α-phase, while the peak corresponding to the polar β-phase becomes more prominent. This modification, highlighted by the deconvolution of the XRD peaks, indicates a progressive enhancement of the β-phase as the concentration of BCZT increases. For a composite containing 10 wt% BCZT, the β-phase peak appears significantly more intense, while the α-phase peak shows a marked decrease, signaling a partial transformation from the α-phase to the β-phase. This transition improves the piezoelectric properties of the composite, enhancing its capacity to convert mechanical vibrations into electrical signals [41].

This improvement in piezoelectricity provides a notable advantage for flexible antennas: in addition to their ability to transmit and receive RF signals, these antennas can also capture and transform mechanical

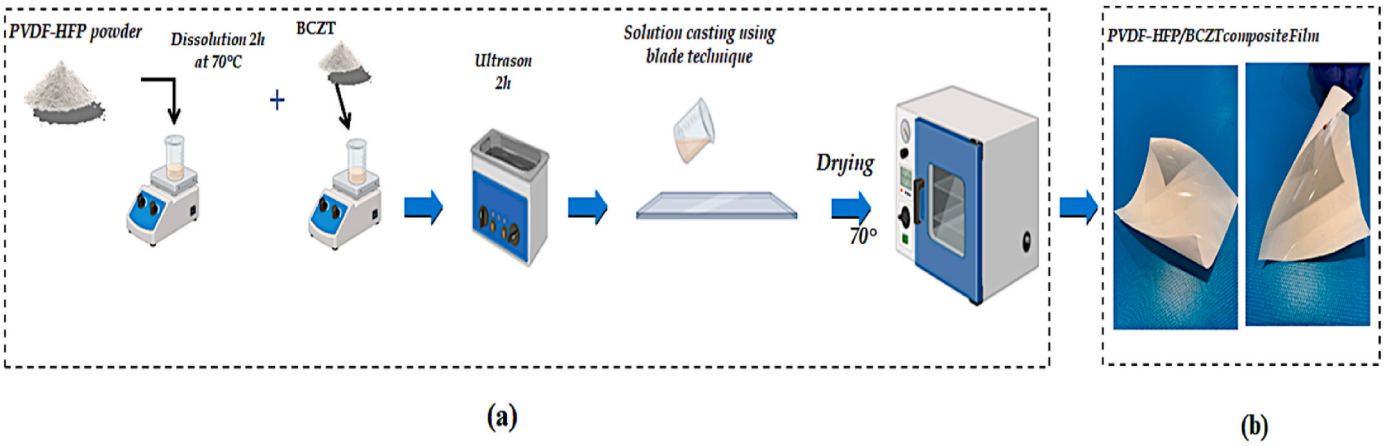

Fig. 1. Schematic representation of the solvent casting method for PVDF-HFP/BCZT films. (a) Flowchart of the fabrication process. (b) Photograph of the final composite film sample.

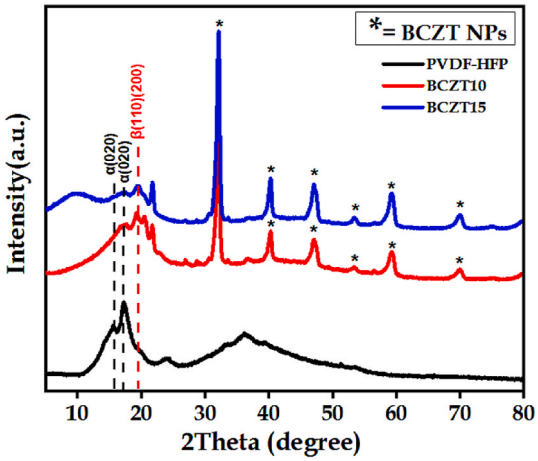

Fig. 2. XRD patterns of pure PVDF-HFP and PVDF-HFP/BCZT composite materials.

vibrations into electrical energy, making them ideal for dynamic environments. The use of polymers as antenna substrates, particularly composites like PVDF-HFP incorporating piezoelectric materials such as BCZT, offers undeniable benefits: flexibility, responsiveness to vibrations, and lightweight characteristics. The development of these flexible antennas based on piezoelectric polymers opens new perspectives for portable devices, integrated sensors, and embedded systems, where flexibility and lightness are essential to meet the demands for portability and adaptability.

2.2.2. *Thermal stability of composite films*

The thermal stability of the composite materials was analyzed using thermogravimetric analysis (TGA) with a TA Instruments Discovery TGA. Composite films were heated to 700 °C in a nitrogen atmosphere to minimize oxidative degradation, ensuring that observed weight loss and decomposition accurately reflect the intrinsic thermal properties of the composites. This controlled environment allows for a precise assessment of thermal resistance and degradation behavior, which is essential for determining the composite's suitability as a stable substrate for flexible antenna applications across a broad temperature range.

Fig. 3 presents the thermal stability of pure PVDF-HFP and PVDF-HFP/BCZT composites, as observed in TGA and DTG curves. In Fig. 3 (a), the TGA curve shows the weight loss relative to temperature for each sample. The data indicate that the thermal stability of PVDF-HFP improves with the addition of BCZT. Pure PVDF-HFP undergoes significant weight loss starting around 440 °C, associated with the breakdown of carbon-hydrogen, and carbon-fluorine bonds. In contrast, the BCZT10 and BCZT15 composites (containing 10% and 15% BCZT, respectively) show enhanced stability, with decomposition beginning at slightly

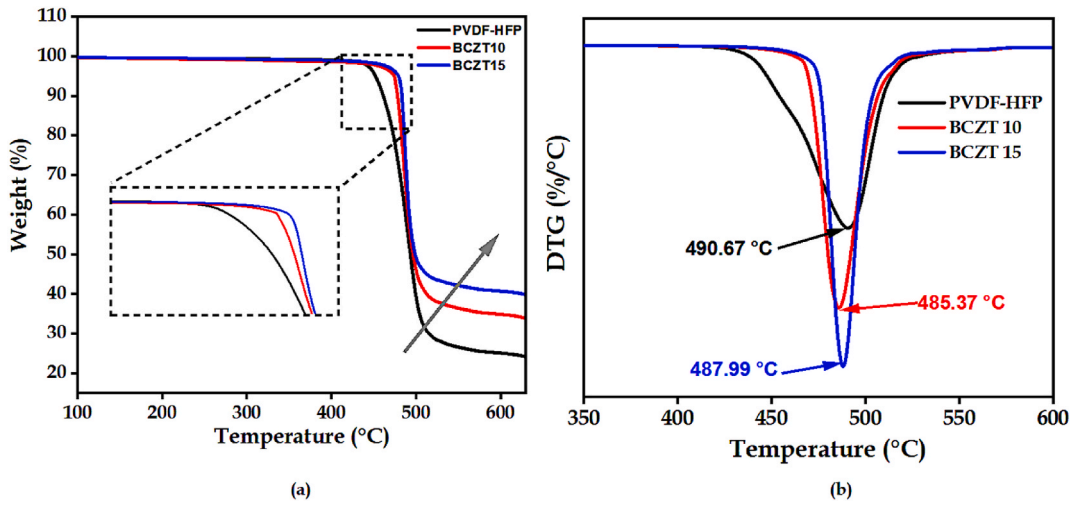

Fig. 3. (a) TGA and (b) DTG curves for pure PVDF-HFP and PVDF-HFP/BCZT composite materials.

higher temperatures. This enhancement suggests that BCZT particles help protect the polymer matrix from degradation by acting as a thermal barrier. In Fig. 3(b), the DTG curve highlights the temperatures at which the maximum rate of weight loss (T_{max}) occurs. The T_{max} values are indicated for each sample, with pure PVDF-HFP at 490.67 °C, BCZT10 at 485.37 °C, and BCZT15 at 487.99 °C. While there is a minor decrease in T_{max} for BCZT10, BCZT15 shows an increase in T_{max} compared to BCZT10, indicating improved thermal stability with higher BCZT content. These findings suggest that incorporating BCZT into PVDF-HFP not only enhances the material's thermal stability but also makes it a promising candidate for use as a substrate in flexible antenna applications. The improved stability may potentially increase the antenna's durability and performance under high-temperature conditions, making it suitable for demanding environments.

2.2.3. Analysis of the mechanical properties of composite films

The mechanical properties of PVDF-HFP composite films reinforced with BCZT particles were analyzed using tensile testing. These tests were conducted at room temperature with a SHIMADZU tensile testing machine in Kyoto, Japan. Rectangular samples with dimensions of 70 mm × 10 mm were tested at a 5 mm/min pulling speed. Each experimental condition was evaluated with a minimum of five samples to ensure data reproducibility and reliability. As shown in Fig. 4(a), the addition of BCZT particles led to a significant increase in Young's modulus. For pure PVDF-HFP, the Young's modulus was measured at 1171 ± 16.3 MPa. When 10% BCZT was incorporated, Young's modulus increased to 1504 ± 12.5 MPa, and with 15% BCZT, it reached 1758 ± 10.3 MPa. This increase indicates a clear reinforcement effect, suggesting that BCZT particles contribute to the rigidity and load-bearing capacity of the composite. In terms of tensile strength, Fig. 4(b) illustrates the improvements achieved by the inclusion of BCZT. The tensile strength of pure PVDF-HFP was 23.71 ± 1.06 MPa, which increased to 28.15 ± 0.22 MPa and 31.07 ± 0.19 MPa for PVDF-HFP/BCZT composites with 10% and 15% BCZT, respectively. This enhancement in tensile strength reflects the efficiency of BCZT particles in strengthening the polymer matrix, allowing it to withstand greater stress without deforming. The improved mechanical properties observed in PVDF-HFP/BCZT composites can be attributed to two main factors. Firstly, the high rigidity and optimal morphology of BCZT particles enable efficient stress transfer within the material, reinforcing the overall structure. Secondly, XRD analyses revealed that BCZT incorporation promotes a partial phase transformation from α-phase to β-phase in the polymer matrix. This β-phase, known for its superior mechanical characteristics, directly enhances both Young's modulus and tensile strength, further supporting the composite's mechanical robustness. Overall, the optimal addition of BCZT at 10% and 15% significantly enhances the mechanical properties of PVDF-HFP, making these composites ideal for applications that require a combination of flexibility and mechanical strength. These properties are especially advantageous for flexible antenna designs, where mechanical durability and effective electromagnetic performance are essential for modern wireless communication systems.

2.2.4. Dielectric test

The dielectric characteristics of the specimens, shaped as circular disks with a 10 mm diameter, were assessed across a frequency span of 100 Hz to 1 MHz at ambient temperature with a dielectric spectroscope (Solartron Analytical).

The electrical properties (permittivity and dielectric loss) of pure PVDF-HFP and its BCZT/PVDF-HFP composite films were evaluated across this frequency range, as shown in Fig. 5. In Fig. 5(a), the dielectric constant increases with the addition of BCZT particles (BCZTPs), particularly as the BCZTP content rises. However, a slight decrease in the dielectric constant is observed as the frequency increases. Notably, when the BCZTP concentration exceeds 10 vol%, a substantial increase in the dielectric constant is recorded. This trend is primarily attributed to the charge polarization at the interface between the BCZT particles and the polymer matrix, as well as the intrinsic dipolar polarization occurring under an alternating electric field. As the frequency varies from 1000 Hz to 1 MHz, a reduction in the dielectric constant is observed. For example, at 1000 Hz, the dielectric constant for the 15 vol% BCZT sample is 18.65, compared to 6.75 for pure PVDF-HFP. This decrease at higher frequencies is likely due to the relaxation of interfacial and dipolar polarization across different frequency ranges [41,42]. The dielectric loss, which measures the energy dissipated through polarization within the material, remains relatively low from 1000 Hz to 10^4 Hz, as shown in Fig. 5(b). The loss tangent remains largely constant within the frequency range of 1000 Hz to 10^5 Hz but experiences a sharp peak around 10^6 Hz. This peak is indicative of the α-relaxation in the PVDF matrix, signifying a glass transition behavior of the polymer at higher frequencies.

The PVDF-HFP/BCZT composite demonstrates significant promise for flexible antenna applications; however, certain limitations and potential errors must be addressed to optimize its performance and reliability. One major challenge is the potential for higher dielectric losses compared to traditional ceramic-based substrates, which could impact antenna efficiency, particularly at higher frequencies. While the addition of BCZT enhances the composite's thermal stability, it remains vulnerable to extreme environmental conditions, such as prolonged exposure to high temperatures or humidity, which could affect its

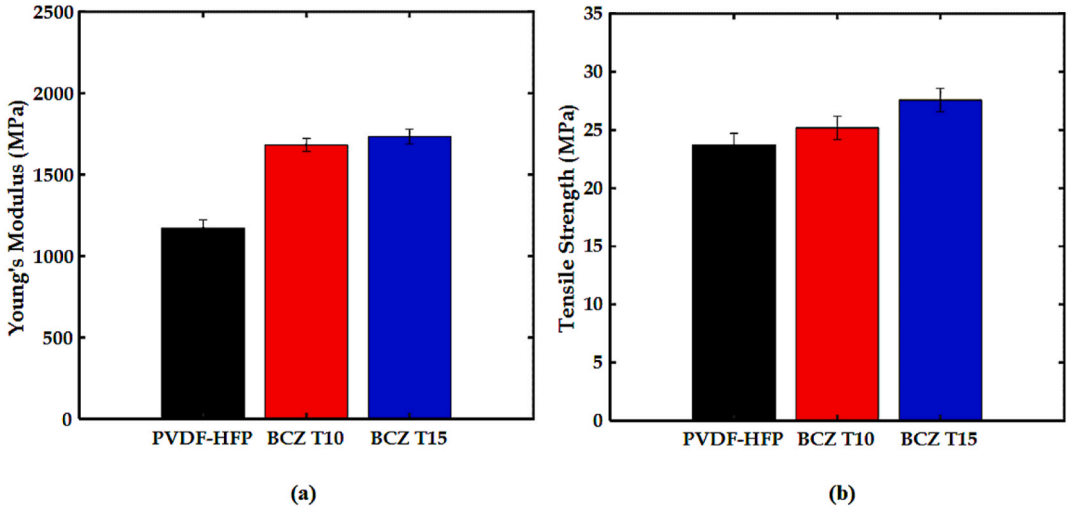

Fig. 4. Tensile properties of pure PVDF-HFP and PVDF-HFP/BCZT composites: (a) Young's modulus and (b) tensile strength for 10% and 15% BCZT additions.

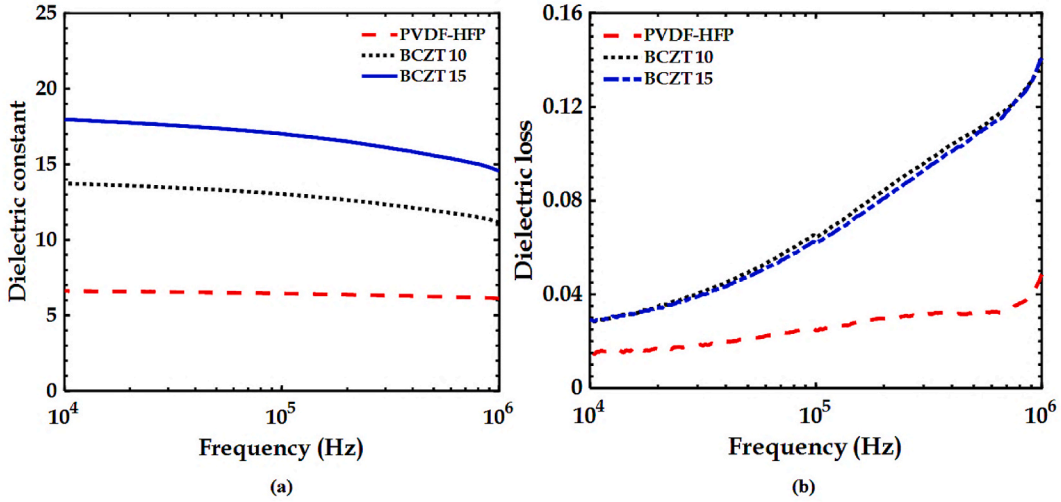

Fig. 5. Electrical characteristics of PVDF-HFP/BCZT composites: (a) Dielectric constant and (b) loss tangent of pure PVDF-HFP compared with PVDF-HFP/BCZT composites at different BCZT concentrations.

functionality and reliability in specific applications. Additionally, the composite's flexibility makes it suitable for wearable devices, but repeated bending or stretching over time may lead to structural fatigue and degradation, ultimately reducing its mechanical durability. From a production perspective, the cost and availability of BCZT particles, coupled with the precise fabrication requirements of the composite, may present barriers to widespread adoption, particularly in cost-sensitive markets. Fabrication processes themselves can introduce errors; for instance, minor dimensional inaccuracies from laser cutting could affect the antenna's resonant frequency and impedance matching. Furthermore, non-uniform dispersion of BCZT particles within the PVDF-HFP matrix could result in uneven dielectric properties, impacting overall performance. The discrepancies between simulated and real-world performance also require careful consideration. Simulation models typically rely on idealized conditions, assuming uniform material properties and perfect boundary conditions, which may not fully align with manufacturing realities. Such differences could lead to variations between simulated predictions and experimental outcomes. Moreover, uncertainties in specific measurement processes, such as SAR evaluation using multilayer human tissue models, might arise due to approximations in replicating real tissue properties. Environmental factors, including fluctuations in temperature and humidity, could further alter the composite's dielectric properties, leading to performance shifts in resonant frequency, return loss, and efficiency. Measurement variability remains another critical issue. The precision of tools like vector network analyzers and anechoic chambers heavily influences the accuracy of parameters such as return loss, VSWR, and radiation efficiency. Additionally, wearable antenna testing on human subjects can yield inconsistent results due to variations in body size, posture, and proximity to the antenna. Practical applications are also prone to electromagnetic interference from surrounding devices, particularly in high-density communication environments, which may distort antenna performance. Future research will focus on addressing these limitations and errors by refining material formulations, optimizing fabrication processes, and enhancing simulation accuracy. Comprehensive reliability tests under diverse environmental and operational conditions will be conducted to develop robust mitigation strategies, ensuring consistent and reliable performance for flexible antenna applications.

3. Antenna modeling and simulation

3.1. Antenna configuration

The antenna configuration presented in Fig. 6 consists of three main elements: the upper radiating element, the intermediate dielectric layer, and the lower electrode functioning as the ground plane. This antenna employs a simplified but efficient structure, featuring a shifted rectangular patch with three strategically placed apertures to improve performance. Additionally, a circular parasitic element is positioned on the opposite side of the dielectric layer to further optimize its functionality. This antenna design has been previously applied as a working antenna in the ultra-wideband spectrum in our earlier research [8]. The antenna's overall size is 30 × 21 × 0.68 mm, contributing to its compact and efficient design. We utilized the ANSYS High-Frequency Structure Simulator (HFSS) 2020 R2, a comprehensive structural simulator based on finite element methods to achieve optimal performance. This advanced simulation tool enabled fine-tuning of the antenna dimensions and analysis of its electromagnetic characteristics, ensuring a robust theoretical foundation for the design. The optimization process involved iterative adjustments of the antenna parameters to meet the desired performance specifications. Table 1 summarizes the key material properties and simulation parameters for the flexible antenna design. It includes the dielectric properties of the PVDF-HFP/BCZT composite, the sheet resistance and thickness of the conductive fabric, as well as the boundary conditions, excitations, and frequency ranges used in the simulation. These factors are essential for optimizing the antenna's performance and ensuring its functionality in practical applications. Table 2 details the final dimensions of the antenna structure, as determined through simulation. This methodology provides a solid theoretical basis for the antenna design, aligning with practical implementation and performance criteria.

3.2. Fundamental equations for electromagnetic simulation

The numerical simulations performed in this work utilized ANSYS HFSS, a widely used electromagnetic simulation tool based on the finite element method (FEM). The governing equations for these simulations are derived from Maxwell's equations, which describe the behavior of electromagnetic fields [43,44]. These fundamental equations are as follows:

Gauss's Law for Electricity

$$\nabla . D = \rho \tag{2}$$

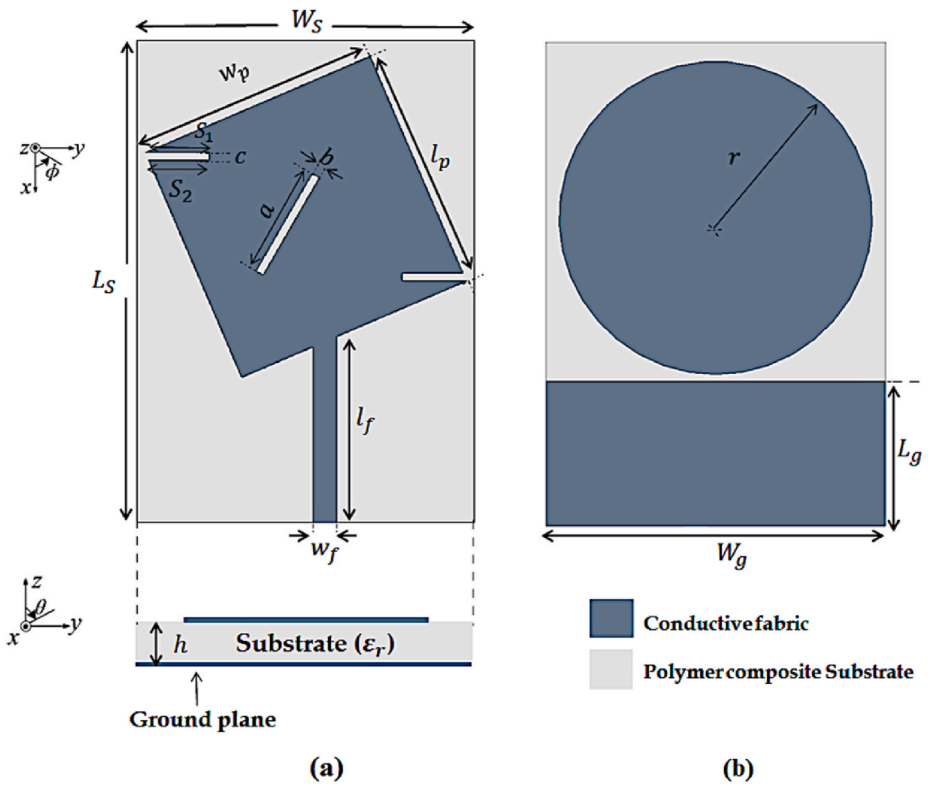

Fig. 6. Configuration and simulation approaches of the proposed flexible antenna: (a) Top view and side view, (b) back view.

Table 1
Summary of simulation setup: Boundary conditions, dielectric parameters, and excitations for the flexible antenna.

Parameter	Description
Boundary conditions	
Open region (radiation)	Defined using the Create open region function to simulate free space.
Substrate bottom	Defined as a perfect ground plane (perfect E boundary).
Dielectric parameters	
Substrate (PVDF-HFP/BCZT)	Relative permittivity (ε_r): 14.58; loss tangent (tanδ): 0.14.
Conductor (patch, ground)	The conductive fabric, has a thickness of 0.09 mm and a sheet resistance of less than 0.05 Ω/sq.
Excitations	
Type	Lumped ports used to excite the system.
Position	Connected between the radiating patch and the ground plane.
Impedance	50 Ω (default).
Simulation frequencies	
Simulated band	4 GHz–8 GHz.
Frequencies of interest	Main resonance: 5.94 GHz; bandwidth: 5.10–6.40 GHz.

Table 2
Optimized dimensions of the antenna design parameters.

Parameter	Value (mm)	Parameter	Value (mm)
W_s	21	l_p	15.23
L_s	30	w_p	15.23
l_g	9	l_f	11.55
w_f	1.5	a	7
b	0.5	S_1	3.97
S_2	4	c	0.5
r	9	t	0.09

Relates the electric displacement field D to the free charge density ρ.

Gauss's Law for Magnetism

$$\nabla .B = 0 \tag{3}$$

Indicates the absence of magnetic monopoles.

Faraday's Law

$$\nabla \times E = -\frac{\partial B}{\partial t} \tag{4}$$

Describes how a time-varying magnetic field induces an electric field.

Ampère's Law (with Maxwell's Addition)

$$\nabla \times H = J + \frac{\partial D}{\partial t} \tag{5}$$

Relates the magnetic field H to the current density J and the time variation of the electric displacement field.

Here, ρ represents the free charge density, J the free current density, and D the electric displacement vector, defined as $D = \varepsilon_0 E + P$, where P is the polarization vector of the medium. The polarization P contributes to the bound charges, with volume charge density $\rho_b = -\nabla \cdot P$ and surface charge density $\sigma_b = -P \cdot n$, where n is the unit normal to the surface.

These equations form the theoretical foundation for the electromagnetic analysis and ensure precise modeling in ANSYS HFSS.

3.3. Antenna designing process

The development of the flexible antenna is methodically outlined through successive modifications intended to improve its performance characteristics. As shown in Fig. 7(a), the initial configuration included a rectangular radiating patch placed on the upper surface of the dielectric substrate, coupled with a full ground plane on the bottom side (Fig. 7(a) (case 1)). This configuration exhibited a frequency range extending from 5.35 GHz to 5.91 GHz and up to 7 GHz, however, it demonstrated

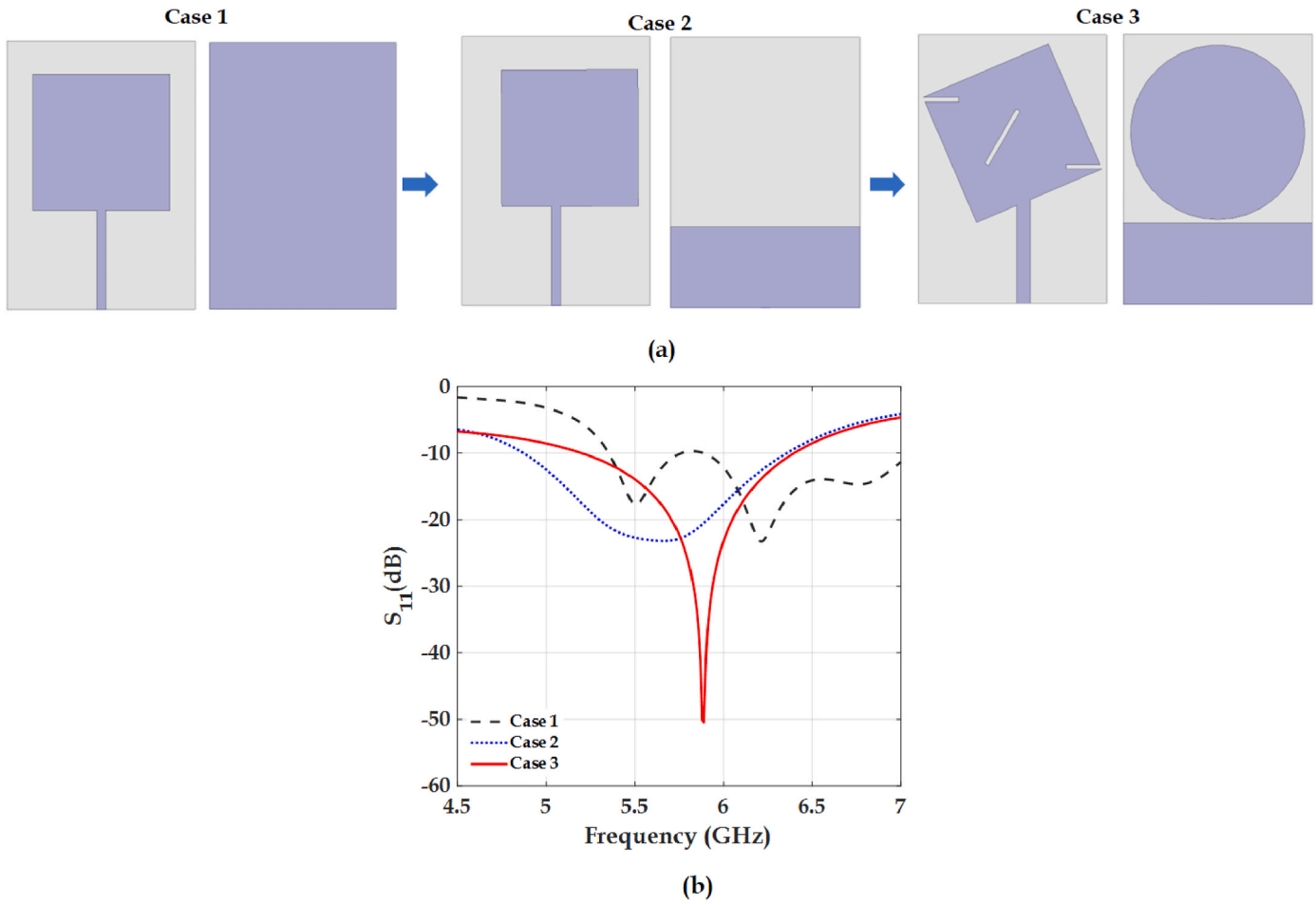

Fig. 7. (a) Evolutionary Stages of the suggested Antenna Design, (b) Simulated Return Loss $|S_{11}|$ for the Evolutionary Stages of the Antenna Design.

suboptimal impedance matching, constraining its performance. The full ground plane was replaced with a partial ground plane to improve impedance matching and bandwidth, resulting in a refined frequency range of 4.87 GHz–6.35 GHz (Fig. 7(a) (Case 2)). Further optimization involved tilting the rectangular patch by 23° and incorporating three slots within the radiating patch. Furthermore, a circular parasitic patch was added to the opposite side of the substrate to reduce rear radiation losses and improve input impedance (Fig. 7(a) (Case 3)). These modifications resulted in a notable enhancement in performance, achieving a broad bandwidth from 5.07 GHz to 6.46 GHz, with a resonant frequency at 5.94 GHz and an impressive return loss of −42.44 dB. The simulated return loss, $|S_{11}|$, for these design iterations is shown in Fig. 7(b), highlighting the transition from suboptimal to highly efficient impedance matching and bandwidth performance. This structured refinement illustrates the antenna's design's clear progression, demonstrating each change's effectiveness in achieving improved bandwidth, impedance matching, and overall efficiency.

In developing the miniaturized patch antenna configuration, the physical dimensions were calculated using equations based on the transmission line model method [45]. Specifically, the patch width (W) is determined by the following equation (6):

$$W = \frac{c}{(2f_r)}\left(\frac{\varepsilon_r + 1}{2}\right)^{-\frac{1}{2}} \tag{6}$$

where c is the speed of light in a vacuum, f_r represents the antenna's resonant frequency, and ε_r denotes the dielectric constant of the substrate.

The patch length (L) is then derived with consideration of the fringe effects, as shown below:

$$L = \frac{c}{2f_r\sqrt{\varepsilon_e}} - 2\Delta L \tag{7}$$

Here, ε_e represents the effective dielectric constant, and ΔL compensates for the elongation of the electric field lines beyond the physical dimensions of the patch.

These calculations facilitate the miniaturization of the antenna while ensuring resonance at the desired frequency, considering the substrate properties and the fringing effects at the patch edges. The derived dimensions can be adjusted to optimize the antenna's performance for specific application requirements.

To thoroughly evaluate the resonant behavior of the monopole antenna, we present the simulation results showing the surface current distribution at the resonant frequency of 5.94 GHz, which corresponds to the TM11 mode of the patch antenna, as shown in Fig. 8(a). At this resonant frequency, the antenna demonstrates a peak current density of 184.93 A/m. The current distribution is primarily focused on the feed line and extends along the boundaries of both the ground plane and the microstrip patch. This localized current density indicates effective coupling between the feed line and the radiating elements, which is essential for the antenna's functionality. The concentration of current along the boundaries of the microstrip patch and ground plane suggests strong interaction in these areas, contributing to the effective radiation and impedance matching of the antenna. The observed distribution confirms the antenna's operational mode and highlights its design effectiveness in achieving the desired resonant frequency. The internal distribution of the electric and magnetic fields within the monopole antenna was thoroughly analyzed. According to the analysis presented

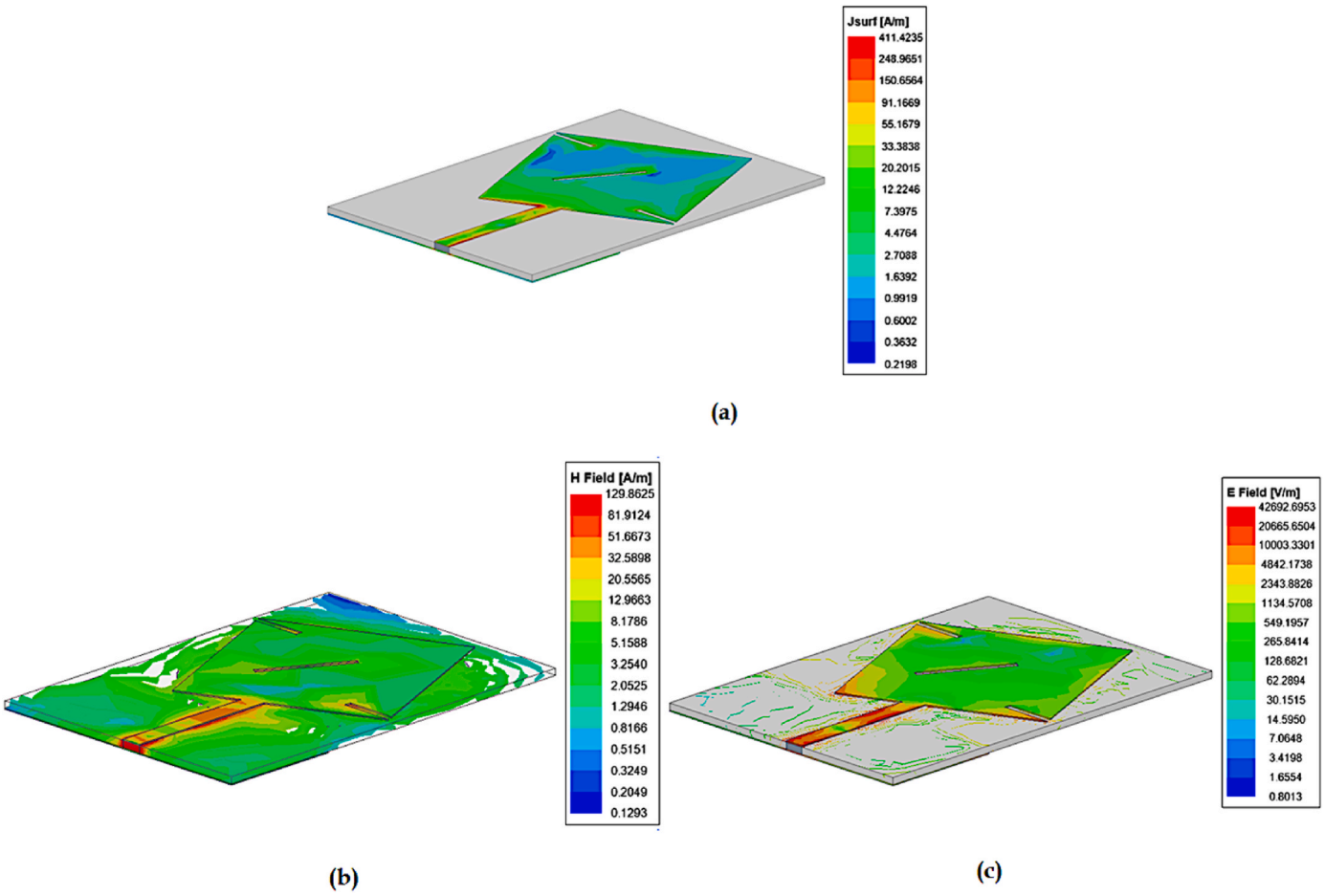

Fig. 8. (a) Distribution of surface current density, (b) electric field distribution, (c) magnetic field distribution at the resonant frequency of 5.94 GHz for the TM11 mode.

in Fig. 8(b), the highest concentration of the electric field is located at the four corners and along the top boundary of the radiating patch. Additionally, a strong electric field is present where the quarter-wavelength impedance transformer connects to the radiating element, as well as at the termination of the 50 Ω impedance adapter. The electric field spreads outward from the edges of the radiating patch, with a particularly noticeable field surrounding the 50 Ω impedance adapter. In Fig. 8(c) the magnetic field distribution is depicted, revealing that the magnetic fields are most intense on either side of the 50 Ω impedance adapter, followed by the edges of the radiating patch. A similar strong magnetic field is also observed at the interface between the quarter-wavelength impedance transformer and the radiating element. These patterns in the electric and magnetic fields suggest that the signal primarily propagates along the edges of the radiating patch. This observation underscores the importance of the patch's role in the overall energy radiation process, as energy predominantly radiates outward from the patch's edges during signal transmission within the microstrip antenna. Consequently, the simulation results are validated, as they accurately reflect the fundamental principles of energy radiation in microstrip antenna design.

3.4. Antenna prototype: fabrication process using laser cutting

To verify the suggested antenna configuration, a prototype was fabricated using precise laser cutting techniques, which were essential for confirming the theoretical model and ensuring its practical feasibility. The prototype utilized a conductive fabric consisting of a blend where copper, nickel, and polyester fibers were combined in proportions of 23%, 20%, and 57%, respectively. This blend was selected due to its excellent electrical conductivity and inherent flexibility as a textile material. The fabric has a thickness of 0.09 mm and boasts an impressively low sheet resistance, below 0.05 Ω/sq, which is essential for ensuring the antenna's optimal performance and long-lasting durability.

The detailed derivation between square resistance and conductivity is as follows:

When the film sample to be measured has a length L, width W, and thickness d, with L = W, the square resistance R_S is defined as:

$$R_S = \frac{\rho.L}{S} = \frac{\rho.L}{W.d} = \frac{\rho}{d} \tag{8}$$

Using the measured square resistance and thickness of the conductive fabric, the conductivity k can be determined with the following equation:

$$k = \frac{1}{\rho} = \frac{1}{R_s.d} \tag{9}$$

The fabrication process employed a Boye Laser GC-1390L cutter for the precise cutting of the conductive fabric layers, an advanced technique that ensures both high accuracy and efficiency, thereby reducing production time and costs. As shown in Fig. 9(a), the laser cutting enabled the creation of intricate geometries essential for the antenna's conductive elements. Following the cutting, the adhesive-backed conductive layers were affixed to the composite film substrate. The assembly, illustrated in Fig. 9(b), involved multiple steps: first, the monopole antenna was mounted onto the upper layer of the substrate. The ground plane and the circular parasitic patch were then positioned

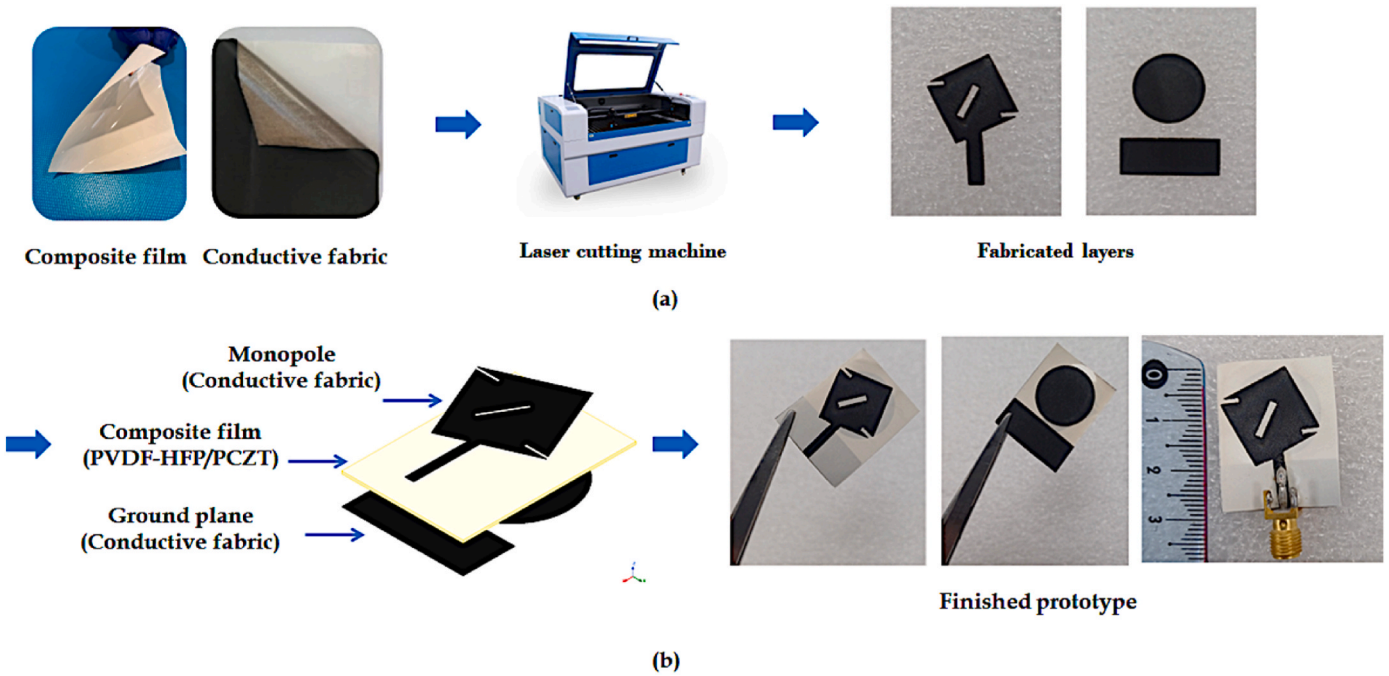

Fig. 9. Antenna prototype assembly process (a) precision laser cutting of conductive fabric layers (b) integration of antenna components and SMA connector attachment.

on the underside of the substrate's bottom layer. Lastly, a SubMiniature Version A (SMA) connector was attached to the transmission line and the back of the antenna, allowing it to interface with a VNA for performance evaluation.

4. Antenna performance and discussion

4.1. Antenna performance evaluation in free space

4.1.1. Input impedance

In this study, the return loss parameter S_{11} is analyzed using a ROHDE & SCHWARZ ZNLE 14 Vector Network Analyzer (VNA). This parameter quantifies the ratio of the power reflected from the antenna to the power entering it and is typically expressed in decibels (dB) as follows [46]:

$$S_{11}(dB) = 10\log_{10}\frac{P_{reflected}}{P_{incident}} \tag{10}$$

Bandwidth is a key factor in assessing antenna performance, as it defines the frequency range over which the antenna can reliably transmit and receive signals. This is typically characterized by the reflection loss (RL) being below 10 dB, indicating minimal signal reflection and efficient energy radiation. The broader the bandwidth, the more versatile the antenna is in handling varying frequencies, which is particularly important for applications requiring multi-frequency operation. At resonant frequencies, the antenna achieves optimal performance with minimal impedance, functioning as a structural resonator. An antenna's resonant behavior is primarily determined by its physical dimensions, which are directly related to its resonant frequency or wavelength. Resonance generally occurs when the antenna length is approximately one-quarter of the wavelength corresponding to the operating frequency. This quarter-wavelength resonance maximizes the radiation efficiency and ensures stable impedance matching, which is critical for achieving high-performance antenna designs. By optimizing both the bandwidth and the resonant frequency, the antenna can be tailored to specific applications, ensuring efficient operation across the desired frequency ranges while maintaining minimal energy loss and enhanced radiation performance. The experimental setup for measuring the reflection coefficient and VSWR, which includes the VNA, is shown in Fig. 10. Fig. 11(a) presents a comparison between simulated and experimental reflection coefficient (S_{11}) results. The simulated reflection coefficient $|S_{11}|$ exhibits a bandwidth spanning 5.07 GHz–6.46 GHz, corresponding to a relative bandwidth of 24.11%. Conversely, the experimental results indicate a narrower bandwidth from 5.5 GHz to 6.17 GHz, yielding a relative bandwidth of 11.48%. The observed discrepancies between simulation and measurement can be attributed to minor fabrication imperfections, such as antenna construction inaccuracies, soldering inconsistencies, or slight differences in material properties from those assumed during simulation. Despite these variations, the comparison between the two simulation tools, including CST Microwave Studio (CST MS), shows a high degree of agreement, particularly in the overall shape and depth of the S_{11} curves across the frequency range. Both simulations verify the antenna's capability to achieve wide bandwidth with minimal return loss across its operating frequencies. Although the measured bandwidth is slightly narrower than

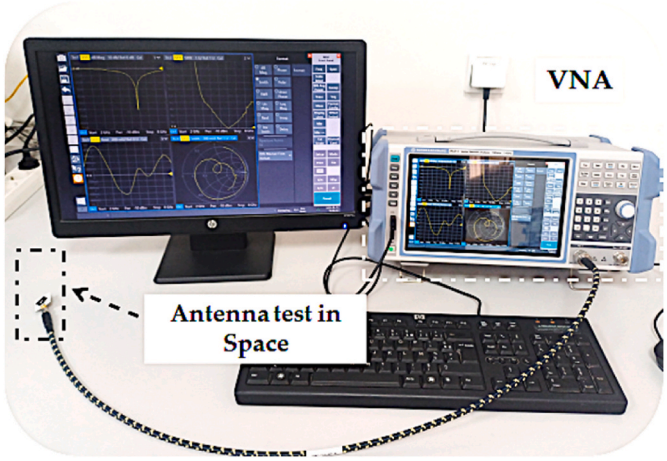

Fig. 10. Experimental setup for reflection coefficient and VSWR measurement using VNA.

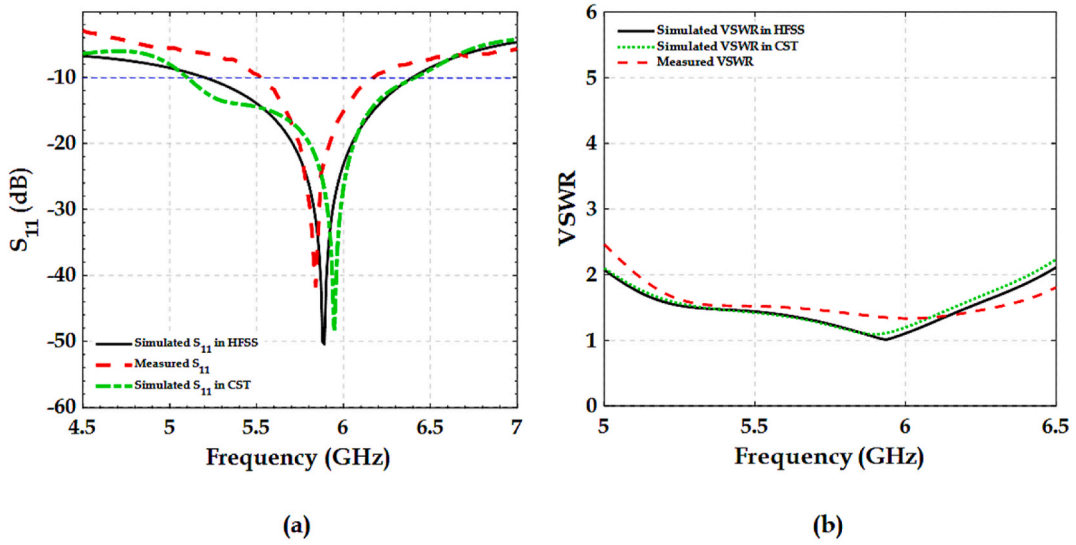

Fig. 11. (a) Simulated and measured reflection coefficient (S_{11}), (b) VSWR across the operating frequency range of the flexible BCZT/PVDF-HFP antenna.

the simulated results, their close alignment highlights the design's reliability and suitability for practical applications. These findings demonstrate that the antenna design is well-optimized for broadband functionality, with return loss values confirming effective impedance matching over the intended frequency range. Minor differences between experimental and simulated outcomes could be minimized with further refinements in the fabrication process, enhancing accuracy in future design iterations.

The Voltage Standing Wave Ratio (VSWR) is a crucial metric in antenna design and operation, representing the extent of impedance matching between the antenna and the feed line. A lower VSWR indicates better impedance matching, with the ideal value approaching 1. Equation (11) provides the formula for calculating VSWR, highlighting the relationship between energy loss due to mismatch and the degree of impedance discontinuity [47]:

$$VSWR = \frac{1 + |S11|}{1 - |S11|} \tag{11}$$

The parameter S_{11} represents the reflection coefficient at the resonant frequency, with values ranging from 0 to 1. When S_{11} is close to 0, the VSWR approaches 1, indicating that nearly all of the input power is efficiently transferred from the feed line to the antenna. Conversely, as S_{11} approaches 1, the VSWR rises sharply, meaning a significant portion of the power is reflected from the antenna's radiating surface. In practical applications, a VSWR between 1 and 2 is generally considered acceptable, as it indicates minimal power loss due to impedance mismatch.

This study analyzed VSWR values across the frequency band from 5.07 GHz to 6.46 GHz, demonstrating that the antenna achieves satisfactory impedance matching for real-world use. Fig. 11(b) illustrates that the VSWR reaches an optimal value of 1.35 at 5.94 GHz, corresponding to minimal reflected power and peak antenna performance at this frequency. This low VSWR confirms that the fabricated antenna meets the design criteria, particularly for 5.8 GHz WLAN applications, ensuring high efficiency and reliable performance. As a result, the antenna is well-suited for practical deployment, offering robust impedance matching and minimal energy loss across the operational bandwidth.

4.1.2. *Far-field characteristics*

Radiation patterns depict how the antenna's radiated power varies with direction in the far-field region. Fig. 12 illustrates the simulated realized gain and radiation efficiency of the antenna. The red curve in the figure shows that the antenna consistently maintains a radiation

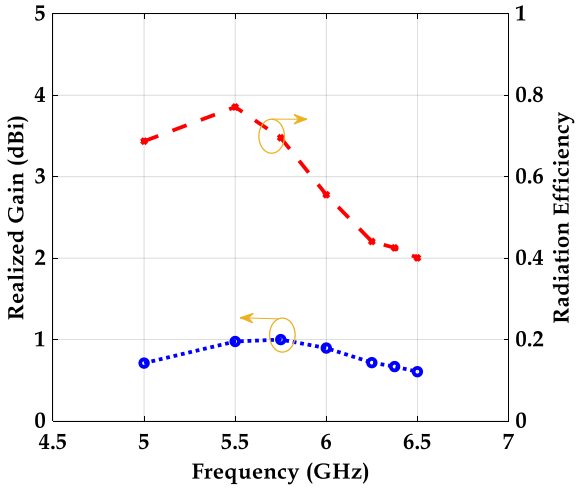

Fig. 12. Realized gain and radiation efficiency of the proposed antenna across the frequency range.

efficiency above 30%, peaking at 37% at 5.95 GHz. The radiation efficiency remains robust across the 5.07–6.46 GHz frequency band, exceeding 50% for most of the range and reaching a maximum of 58% at the resonant frequency of 5.94 GHz. These results highlight the antenna's ability to sustain high efficiency over a wide frequency spectrum, demonstrating its suitability for broadband wearable applications.

The observed reduction in efficiency can be primarily attributed to the losses inherent in the substrate layers, including the PVDF-HFP/BCZT composite substrate and the conductive textile, as well as the dimensions of the antenna. To significantly enhance radiation efficiency, future work should explore the use of substrates with lower loss properties and textiles with improved conductivity. Additionally, optimizing the antenna design to achieve a more uniform current distribution across its structure could further augment efficiency. Addressing these aspects will be essential for advancing the practical performance of the antenna in real-world applications [48,49]. The antenna's realized gain, as depicted in Fig. 12 (blue curve), shows a peak value of approximately 0.67 dBi at the resonant frequency. This gain level reflects the antenna's ability to radiate power efficiently. However, a major limitation of the current configuration is its relatively low radiation efficiency, which is directly linked to the observed low gain. Several factors contribute to

this suboptimal performance. First, the insufficient conductivity of the conductive textile used in the antenna's construction restricts effective power transfer.

Secondly, the thinness of the substrate further exacerbates this issue by restricting the antenna's ability to support efficient radiation. Most notably, the high dielectric loss associated with the proposed substrate material results in elevated values of quality factors such as Q_r, Q_c, and Q_d. Specifically, these quality factors correspond to radiation loss, conductive loss, and dielectric loss, respectively. The high dielectric loss contributes to a high Q_r, which in turn adversely affects both Q_c and Q_d, leading to overall reduced efficiency [50]. This results in a decrease in efficiency and gain. This observation can be validated through CST simulation. By reducing the loss tangent (tanδ) to values like 0.05 or 0.04, the realized gain of the antenna can be improved, reaching up to 1 dBi within the resonance band. Additionally, increasing the substrate thickness proves beneficial in enhancing radiation efficiency and further boosting the gain. Addressing these limitations requires targeted improvements in material selection and design modifications. Enhancing the fabric's conductivity, increasing the substrate thickness, and selecting materials with lower dielectric loss are potential strategies to improve the antenna's radiation efficiency. Future work will focus on these areas to achieve a more efficient and higher-performing antenna design.

Fig. 13(a) and (b) present the two-dimensional (2D) and three-dimensional (3D) radiation patterns of the proposed flexible antenna, respectively. Fig. 13(a) displays the 2D radiation patterns at the resonant frequency of 5.94 GHz for the E-plane and H-plane. The E-plane pattern, represented by the red dashed line, displays a directional behavior with notable gain in the forward (0°) and backward (180°) directions, indicating strong radiation efficiency in these lobes. However, the radiation strength decreases significantly at side angles (±90°). In contrast, the H-plane pattern, depicted by the blue dotted line, exhibits a nearly omnidirectional radiation characteristic, with minor variations in strength at different angles, as indicated by subtle ripples. Despite these variations, the antenna maintains uniform performance across the plane. Fig. 13(b) presents the 3D directivity pattern of the antenna at 5.94 GHz. The antenna exhibits a well-defined directional radiation pattern, with a dominant lobe emerging from the patch. This configuration underscores the antenna's ability to focus energy in specific directions, making it well-suited for applications that require precise signal targeting.

4.2. Assessment of antenna performance with body interaction

To comprehensively assess the performance of the suggested antenna in realistic wearable scenarios, simulations were carried out in both free space and on a body phantom. Given that portable antennas are intended to function near the body, evaluating their behavior solely in free space provides only limited insight. A more accurate representation of its operational characteristics in practical applications can be obtained by simulating the antenna's interaction with a human body phantom. The human body introduces additional dielectric loading, detuning, and absorption effects that must be accounted for in antenna performance evaluations. For this study, a multilayer human tissue model was developed, comprising layers of skin, fat, muscle, and bone, as shown in Fig. 14. The phantom's dimensions (150 mm × 150 mm × 39 mm) were selected to balance computational efficiency with accuracy. This configuration ensures that the separation between the antenna and the phantom's boundary exceeds one-quarter wavelength at 5.8 GHz, mitigating boundary-related artifacts in the simulation. The electromagnetic properties of each tissue layer at 5.8 GHz, along with their respective thicknesses, are provided in Table 3 [51], ensuring precise modeling of the human body's electromagnetic response. A 10 mm air gap was maintained between the antenna and the surface of the

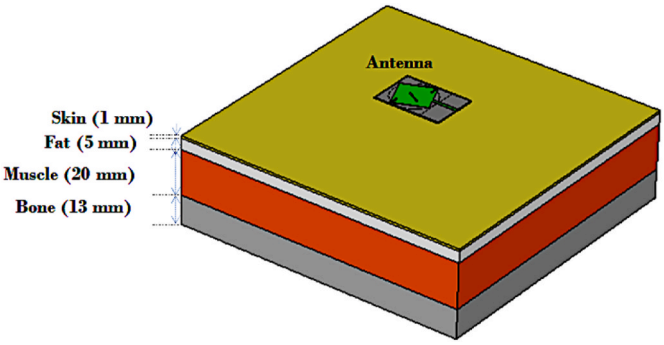

Fig. 14. Multilayer human tissue model for antenna performance simulation.

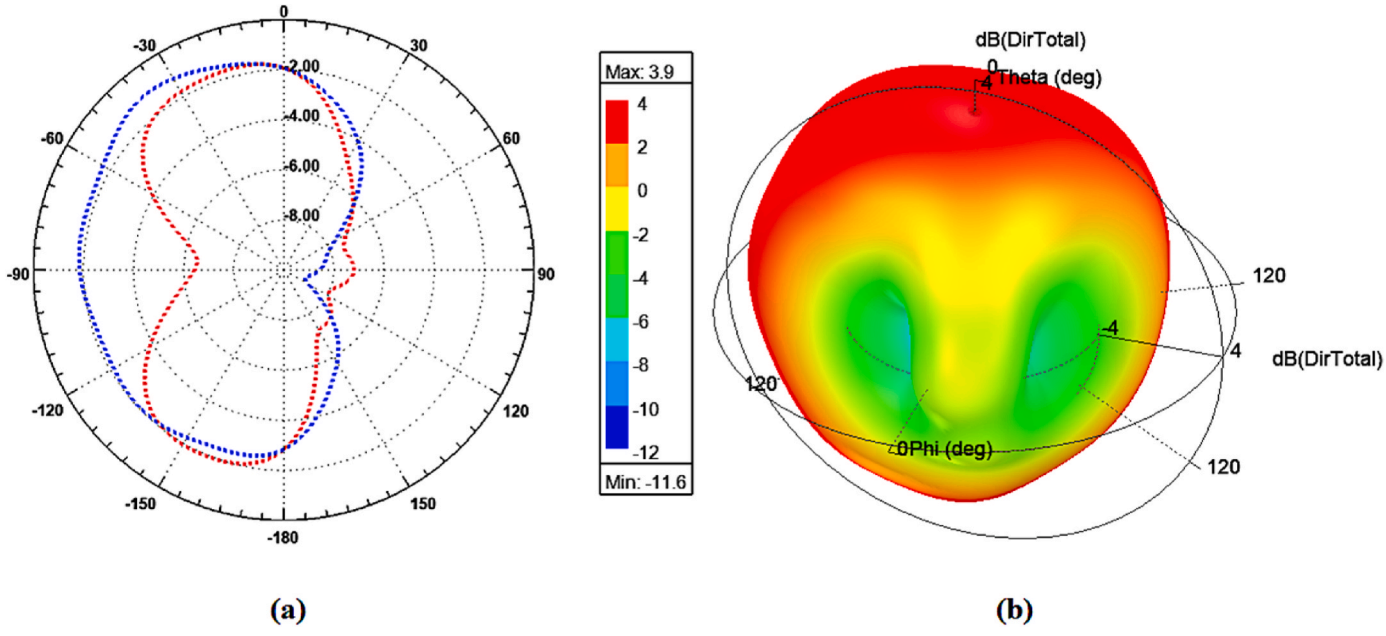

Fig. 13. Simulated 2D radiation patterns at 5.94 GHz (a) and 3D directivity pattern at 5.94 GHz (b) of the proposed BCZT/PVDF-HFP-based flexible antenna.

phantom, simulating realistic placement scenarios where the antenna is separated from the body by a layer of clothing or other materials. This spacing is critical for reproducing typical wearable antenna environments.

Experimental validation was performed with a male volunteer (height: 1.9 m, weight: 63 kg), depicted in Fig. 15(a). The reflection coefficient ($|S_{11}|$) was directly measured on the human body with a VNA. This setup enabled a direct comparison between the simulated and experimental results, offering valuable insights into the antenna's performance in practical scenarios. The measured $|S_{11}|$ values, compared with the simulated data, are shown in Fig. 15(b), highlighting strong agreement between the two datasets. When simulated on the human body phantom, the antenna exhibited an impedance bandwidth of 36.6% (4.60–6.65 GHz) for $|S_{11}| < -10$ dB. However, measurements taken directly on the human body revealed a reduced bandwidth of 22.0% (4.84–6.04 GHz), attributable to the increased dielectric loading and absorption effects of human tissues. This bandwidth reduction is consistent with expectations for wearable antennas and highlights the importance of accounting for body loading in performance evaluations. Despite the decrease in bandwidth, the antenna maintained satisfactory performance, confirming its suitability for wearable applications operating within this frequency range. These findings underscore the necessity of evaluating antenna performance under conditions that closely replicate real-world scenarios. The proposed antenna exhibits strong performance when mounted on the human body, positioning it as an excellent option for integration into body-worn systems that demand reliable operation in wearable environments.

4.3. Evaluation of wearable safety

A primary concern for wearable antennas in body-centric wireless networks is the interaction of electromagnetic energy with human tissues. This energy absorption is quantified by the Specific Absorption Rate (SAR), which gauges the rate at which the body absorbs radio frequency (RF) energy from wireless devices. The European Union (EU) has established a SAR limit of 2 W/kg, averaged over 10 g of tissue, to regulate exposure to electromagnetic fields. Simulations were carried out using a planar tissue model that mimics human body conditions to evaluate the SAR of the proposed antenna. The SAR is determined using Equation (12):

$$SAR = \frac{\sigma \left| \vec{E} \right|^2}{\rho} \tag{12}$$

where:

σ denotes the tissue's electrical conductivity (S/m), E represents the magnitude of the electric field (V/m), and ρ refers to the mass density of the tissue (kg/m^3).

Fig. 16 illustrates the simulated SAR distribution for the proposed antenna, which was positioned 10 mm above the tissue model with an input power of 0.5W. The antenna design features a fully shielded reverse side and is intended for integration into garments such as coats, which inherently provide a separation of at least 5–10 mm from the body. This separation, achieved either through the garment or a non-conductive spacer, significantly reduces electromagnetic exposure to human tissues, enhancing the safety and usability of the device during extended periods of wear. By maintaining this distance, the antenna's design minimizes the impact of tissue proximity on its performance and ensures that no biocompatibility concerns arise in the intended wearable applications. SAR evaluations were conducted according to international safety standards for two tissue masses—1 g and 10 g—widely accepted measures for assessing localized and distributed energy absorption in wearable devices. The simulation results showed a SAR value of 1.12 W/kg for 1 g of tissue, which is well beneath the Federal Communications Commission (FCC) limit of 1.6 W/kg. This confirms safe operation regarding localized tissue energy absorption. For the 10 g tissue mass, the SAR value decreased to 0.366 W/kg, well under the European Union (EU) standard limit of 2 W/kg. This indicates lower, more uniform energy absorption across a larger tissue volume. These findings validate that the proposed antenna adheres to both FCC and EU safety regulations, positioning it as a viable option for wearable technologies. The design effectively minimizes electromagnetic exposure while maintaining reliable performance, ensuring it is safe and appropriate for long-term use in wearable devices.

4.4. Performance comparison

Table 3 presents a comprehensive comparative analysis of the suggested antenna's performance in comparison to other advanced flexible substrate portable antennas reported in the literature. This comparison evaluates critical parameters, including materials, operating frequencies, return loss, bandwidth, dielectric permittivity, and dielectric loss at 1 MHz. As indicated in Table 3, the suggested antenna functions at a frequency of 5.94 GHz with a bandwidth of 1300 MHz. which is competitive with antennas operating at other frequencies, such as [29] (1.26–6.17 GHz) and [52] (0.828–8.73 GHz). While higher-frequency

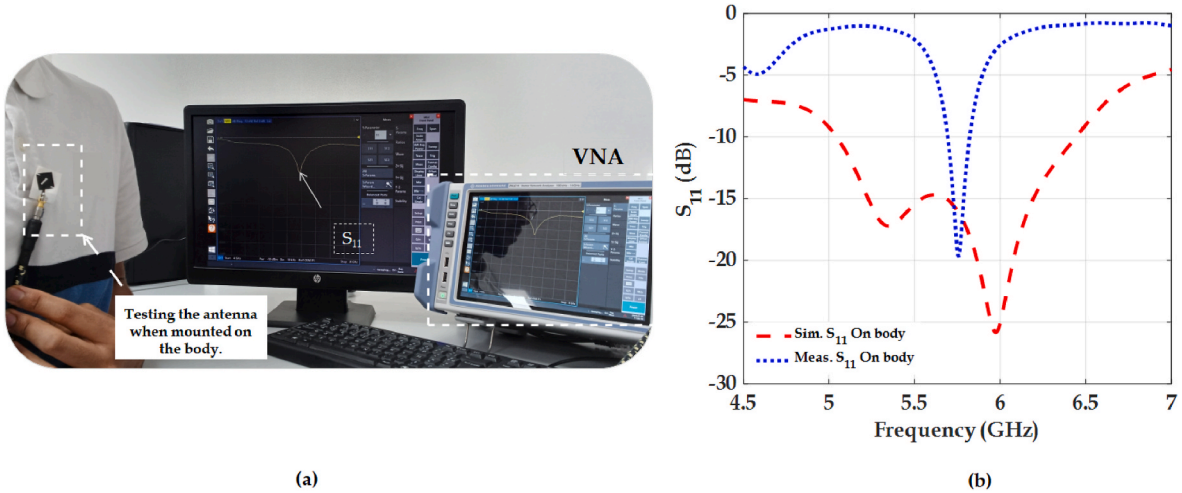

Fig. 15. (a) Experimental setup for measuring antenna performance on a human volunteer using vector network analyzer. **(b)** Comparison of simulated and measured reflection coefficient ($|S_{11}|$) for the suggested antenna in free space and on the human body.

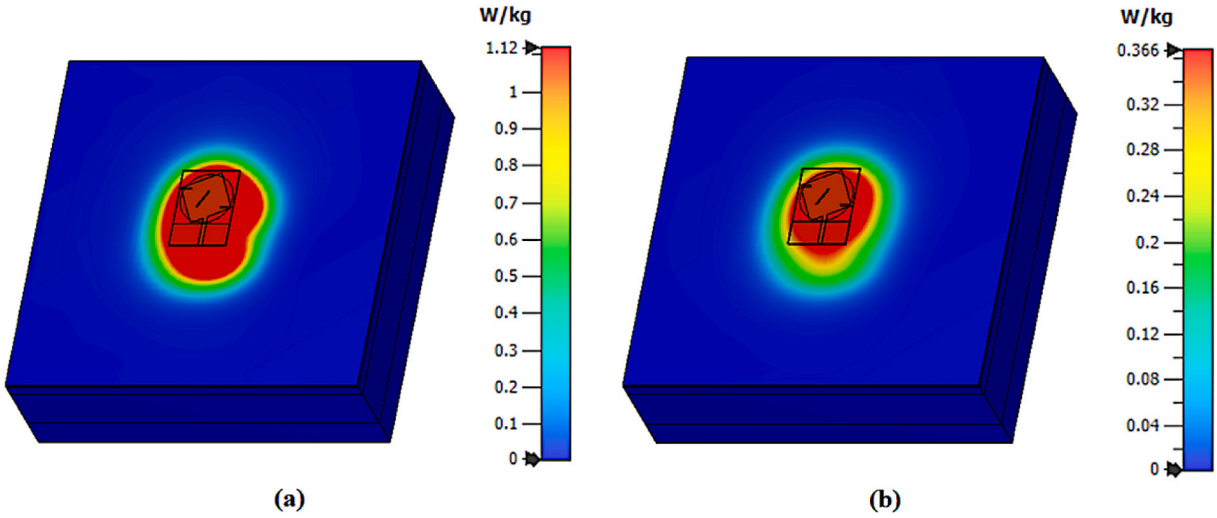

Fig. 16. Simulated specific absorption rate (SAR) distribution of the antenna on a body model at 5.8 GHz: (a) SAR for 1 g of tissue and (b) SAR for 10 g of tissue.

Table 3
Dielectric properties and thickness of human tissue layers at 5.8 GHz.

Tissue	5.8 GHz		Thickness (mm)
	ε_r	σ (s/m)	
Skin	35.1	3.72	3
Fat	4.9	0.33	7
Muscle	48.4	4.9	20
Bone	15.39	2.14	10

antennas tend to achieve narrower bandwidths, the suggested antenna provides a strong balance of bandwidth and frequency that is well-suited for 5G applications. This wide bandwidth offers advantages in data throughput and multifunctional performance, making it competitive for next-generation communication systems. The proposed antenna demonstrates an exceptional return loss of −48.32 dB, significantly surpassing most comparable designs in the literature. For instance, the return losses reported in Ref. [53] range from −20.8 dB to −41.2 dB, while [54] achieves a return loss of only −21.23 dB. This remarkable improvement in return loss highlights the superior impedance matching and reduced signal reflection characteristics of the proposed antenna, contributing to enhanced signal transmission efficiency.

At 1 MHz, the dielectric permittivity of the P(VDF-HFP)/BCZT composite substrate employed in the suggested antenna is measured at 14.58. The dielectric permittivity of 14.58 at 1 MHz is moderate, contributing to the antenna's balance between electrical performance and flexibility. Higher permittivity materials, like the 21.52 reported in Ref. [55], may improve electrical performance but could compromise flexibility, which is critical for wearable applications. This trade-off in dielectric properties ensures the proposed material remains suitable for flexible, wearable electronics. The dielectric loss of this material is relatively low at 0.14, indicating minimal energy dissipation during signal propagation. Furthermore, the low dielectric loss ensures minimal signal energy is lost as heat, which is particularly important for maintaining efficiency in wearable devices, where power consumption and heat dissipation are constraints. Overall, Table 4 highlights various materials used in flexible antennas, showing how trade-offs between dielectric properties and mechanical flexibility influence performance. For instance, while the $ZnAl_2O_4Ca$ substrate in Ref. [56] achieves excellent dielectric permittivity (21.52), its brittleness makes it less practical for wearable devices. In contrast, P(VDF-HFP)/BCZT offers moderate permittivity and low dielectric loss, balancing flexibility and performance, which is crucial for wearable applications. The P(VDF-HFP)/BCZT composite emerges as a superior choice, characterized by a unique combination of performance attributes that make it highly suitable for dynamic, flexible applications in the rapidly expanding field of wearable electronics.

Table 4
Comparative analysis of developed antennas.

Ref	Material	Operating freq.	Return loss (dB)	Bandwidth (MHz)	Dielectric permittivity@1 MHz	Dielectric loss @1 MHz
[29]	PMMA/PVDF-HFP/PZT	1.26–6.17	–	4910	5.13	0.03
[53]	MnxZn (1-x) Fe_2O_4	4.8	−27.4	1800	4.74–6.06	–
		4.4	−41.2	2000		
		4.2	−20.8	1600		
		4.6	−23.3	2400		
		4.6	−22.9	2600		
[56]	ZnAl2O4Ca	6.7	−32.38	760	21.52	0.021
[55]	ZnAl2O4Ca	6.80	−20.92	600	21.11	0.024
[54]	$CaCu_3Ti_4O_{12}$	2.45	−21.23	540	447	0.42
[57]	Bi_4Ti3O_{12}	2.45	−4.95	–	450	0.98
[52]	$0.9ZnAl_2O_40.1(0.6\ wt\%V_2O_5\text{-}0.4\ wt\%\ TiO_2)$	0.828	−12.95	0.618	22.82–22	0.14–0.007
		2.21	−12.33	319		
		4.22	−18.69	1270		
		7.26	−31.46	1465		
		8.73	−44.69	1723		
Present work	**P(VDF-HFP)/BCZT**	**5.94**	**−48.32**	**1300**	**14.58**	**0.14**

5. Conclusion

In conclusion, this research presents the successful design, fabrication, and assessment of an innovative flexible wideband antenna that uses a composite substrate composed of PVDF-HFP and Barium BCZT, with a conductive fabric as the radiating element. The integration of BCZT particles within the PVDF-HFP matrix notably enhanced the dielectric properties, thermal stability, and mechanical robustness of the substrate, highlighting its potential for wearable antenna applications. The potential of the PVDF-HFP/BCZT composite as a substrate for microwave applications was confirmed through the fabrication and testing of a microstrip patch antenna optimized for WLAN systems. The proposed antenna's electromagnetic performance was analyzed via simulations conducted in ANSYS HFSS and verified by CST Microwave Studio, followed by experimental testing using a VNA. Simulation outputs from both HFSS and CST supported the modeling of the antenna's electromagnetic characteristics and allowed an in-depth analysis of its radiation processes. The close match between simulated and measured results affirms the precision of the electromagnetic simulation approach and offers valuable insights into the antenna's radiation properties. Both simulation and experimental data validated that the antenna functions efficiently within the 5.10–6.40 GHz frequency spectrum, achieving a return loss of −48.32 dB and maintaining a VSWR below 2. Specific Absorption Rate (SAR) values, recorded at 1.22 W/kg (1g) and 0.366 W/kg (10g), were well within global safety limits, indicating the antenna's safe application on the body. To our knowledge, this work is, the first application of a PVDF-HFP/BCZT composite in wearable antennas, showcasing its promise as an environmentally friendly and flexible option for future wearable communication devices. The strong alignment between the simulation and experimental findings emphasizes the reliability and effectiveness of this composite antenna design. This research lays the foundation for lightweight, flexible, and high-performance antennas that meet the expanding requirements of wearable and IoT technologies. Future studies will focus on optimizing the antenna design for multi-band functionality and investigating energy-harvesting integration to improve the autonomy of wearable systems.

CRediT authorship contribution statement

Saïd Douhi: Conceptualization, Methodology, Software, Data curation, Visualization, Formal analysis, Validation, Writing – original draft. **Salesabil Labihi:** Conceptualization, Methodology, Software, Visualization, Validation. **Adil Eddiai:** Conceptualization, Methodology, Data curation, Validation, Supervision , Resources, Project administration, Writing – review & editing. **Soufian Lakrit:** Methodology, Software, Visualization, Validation. **Mounir El Achaby:** Conceptualization, Methodology, Visualization, Validation, Writing – review & editing. **Ahmed Jamal Abdullah Al-Gburi:** Writing – review & editing, Project administration, Funding acquisition.

Declaration of competing interest

The authors declare that they have no known competing financial interests or personal relationships that could have appeared to influence the work reported in this paper.

Acknowledgement

The authors express their gratitude to the Moroccan Ministry of Higher Education, Scientific Research, and Innovation, as well as the Office Cherifien des Phosphates (OCP S.A.) Foundation, for their support and funding the APRD research program. Additionally, they extend their thanks and acknowledge the support and funding provided by Universiti Teknikal Malaysia Melaka (UTeM), the Centre for Research and Innovation Management (CRIM), and the Malaysian Ministry of Higher Education (MOHE).

References

[1] M. Zhang, P. Xu, H. Peng, F. Qin, A rational design of core-shell-satellite structured BaTiO3 fillers for epoxy-based composites with enhanced microwave dielectric constant and low loss, Compos. B Eng. 215 (2021) 108764, https://doi.org/10.1016/j.compositesb.2021.108764.

[2] K. El Batal, S. Douhi, A. Eddiai, S. Das, O. Cherkaoui, M. Mazroui, Design and performance analysis of a low-profile dual-band antenna with low specific absorption rate using textile materials for wearable and RF energy harvesting applications, J. Electron. Mater. (2024), https://doi.org/10.1007/s11664-024-11455-5.

[3] A.J.A. Al-Gburi, N.H.M. Radi, T. Saeidi, N.J. Mohammed, Z. Zakaria, G.S. Das, A. Buragohain, M.M. Ismail, Superconductive and flexible antenna based on a tri-nanocomposite of graphene nanoplatelets, silver, and copper for wearable electronic devices, J. Sci.: Adv. Mater. Dev. 9 (2024) 100773. https://www.sciencedirect.com/science/article/pii/S2468217924001047. (Accessed 11 November 2024).

[4] A. Abdelrahman, F. Erchiqui, M. Nedil, Fabricated wearable and flexible chip composed strain of gallium and silver metals composites assembled on graphene inside PDMS matrix, J. Indian Chem. Soc. 99 (2022) 100345, https://doi.org/10.1016/j.jics.2022.100345.

[5] S. Zhang, J. Zhu, Y. Zhang, Z. Chen, C. Song, J. Li, N. Yi, D. Qiu, K. Guo, C. Zhang, T. Pan, Y. Lin, H. Zhou, H. Long, H. Yang, H. Cheng, Standalone stretchable RF systems based on asymmetric 3D microstrip antennas with on-body wireless communication and energy harvesting, Nano Energy 96 (2022) 107069, https://doi.org/10.1016/j.nanoen.2022.107069.

[6] A.J.A. Al-Gburi, M.M. Ismail, N.J. Mohammed, A. Burago- hain, K. Alhassoon, Electrical conductivity and mor- phological observation of hybrid filler: silver-graphene oxide nanocomposites for wearable antenna, Opt. Mater. 148 (2024) 114882.

[7] S. Douhi, A. Eddiai, T. Islam, S. Das, O. Cherkaoui, M. Mazroui, A compact two-port semi-flexible dual-band circularly polarized MIMO antenna structure for millimeter-wave 26/31 GHz 5G applications, in: M. El Ghzaoui, S. Das, V. Samudrala, N.R. Medikondu (Eds.), Next Generation Wireless Communication, Springer Nature Switzerland, Cham, 2024, pp. 149–160, https://doi.org/10.1007/978-3-031-56144-3_9.

[8] S. Douhi, A. Eddiai, S. Das, B.T.P. Madhav, M. Meddad, O. Cherkaoui, M. Mazroui, Design of a compact super wideband all-textile antenna for radio frequency energy harvesting and wearable devices, Opt. Quant. Electron. 55 (2023), https://doi.org/10.1007/s11082-023-05498-x.

[9] Ahmed Jamal Abdullah Al-Gburi, Mohd Muzafar Ismail, Naba Jasim Mohammed, Thamer A.H. Alghamdi, SAR flexible antenna advancements: highly conductive polymer-graphene oxide-silver nanocomposites, Prog. Electromagn. Res. M 127 (2024) 23–30, https://doi.org/10.2528/PIERM24011202.

[10] MdB. Billa, M.T. Islam, T. Alam, A. Hoque, S. Albadran, H. Alsaif, A.S. Alshammari, A. Alzamil, M.S. Soliman, Morphological, optical, and electrical properties of CoxCa(0.90-x)Ni0.10Fe2O4 based flexible metamaterial substrate for industrial chemical contamination sensing, J. Sci.: Adv. Mater. Dev. 9 (2024) 100659, https://doi.org/10.1016/j.jsamd.2023.100659.

[11] A. Abdelrahman, F. Erchiqui, M. Nedil, B. Aïssa, M. Siaj, Electrically conductive PDMS/Clay nanocomposites assembled with graphene, copper and silver nanoparticles for flexible electronic applications, J. Electroceram. 51 (2023) 37–50, https://doi.org/10.1007/s10832-023-00315-z.

[12] A. Boumegnane, S. Douhi, A. Batine, T. Dormois, C. Cochrane, A. Nadi, O. Cherkaoui, M. Tahiri, Rheological properties and inkjet printability of a green silver-based conductive ink for wearable flexible textile antennas, Sensors 24 (2024) 2938, https://doi.org/10.3390/s24092938.

[13] S. Douhi, T. Islam, R.A. Saravanan, A. Eddiai, S. Das, O. Cherkaoui, Design of a flexible rectangular antenna array with high gain for RF energy harvesting and wearable devices. https://essuir.sumdu.edu.ua/handle/123456789/92392, 2023. (Accessed 25 September 2024).

[14] M. Hussain, H. Zahra, S.M. Abbas, Y. Zhu, Flexible dielectric materials: potential and applications in antennas and RF sensors, Adv Elect. Mater. (2024) 2400240, https://doi.org/10.1002/aelm.202400240.

[15] Z. Islam, Polymer-based low dielectric constant and loss materials for high-speed communication network: dielectric constants and challenges, Eur. Polym. J. (2023).

[16] A. Abdelrahman, F. Erchiqui, M. Nedil, S. Mohamed, In situ- preparation and estimation of the physical characterization of Nanofluidic solution and its application, Proceedings of the Institution of Mechanical Engineers, Part N: journal of Nanomaterials, Nanoeng. Nanosys. 238 (2024) 3–16, https://doi.org/10.1177/23977914221127527.

[17] J.-W. Zha, M.-S. Zheng, B.-H. Fan, Z.-M. Dang, Polymer-based dielectrics with high permittivity for electric energy storage: a review, Nano Energy 89 (2021) 106438, https://doi.org/10.1016/j.nanoen.2021.106438.

[18] A. Eddiai, M. Meddad, K. Sbiaai, Y. Boughaleb, A. Hajjaji, D. Guyomar, A new technique for maximizing the energy harvested using electrostrictive polymer composite, Opt. Mater. 36 (2013) 13–17, https://doi.org/10.1016/j.optmat.2013.07.014.

[19] Z. Zhang, J. Zhang, S. Li, J. Liu, M. Dong, Y. Li, N. Lu, S. Lei, J. Tang, J. Fan, Z. Guo, Effect of graphene liquid crystal on dielectric properties of polydimethylsiloxane nanocomposites, Compos. B Eng. 176 (2019) 107338, https://doi.org/10.1016/j.compositesb.2019.107338.

[20] A. Abdelrahman, F. Erchiqui, M. Nedil, S. Mohamed, Enhancing fluidic polymeric solutions' physical properties with nano metals and graphene additives, J. Mol. Liq. 370 (2023) 121052, https://doi.org/10.1016/j.molliq.2022.121052.

[21] N. Hasan, N.H. Noordin, M.S.A. Karim, M.R.M. Rejab, Q.J. Ma, Dielectric properties of epoxy–barium titanate composite for 5 GHz microstrip antenna design, SN Appl. Sci. 2 (2020) 62, https://doi.org/10.1007/s42452-019-1801-9.
[22] A. Mayeen, M.S. Kala, S. Sunija, D. Rouxel, R.N. Bhowmik, S. Thomas, N. Kalarikkal, Flexible dopamine-functionalized BaTiO3/BaTiZrO3/BaZrO3-PVDF ferroelectric nanofibers for electrical energy storage, J. Alloys Compd. 837 (2020) 155492, https://doi.org/10.1016/j.jallcom.2020.155492.
[23] A. Hussain, L. Jie, C. Zhao, J. Yu, A.M. Khan, S. Luo, S. Yu, Low voltage tunability of PVDF-based nanocomposites by interface polarization induced by TiO2-coated BST core-shell nanoparticle, Compos. Commun. 49 (2024) 101984, https://doi.org/10.1016/j.coco.2024.101984.
[24] N. Chakhchaoui, R. Farhan, A. Eddiai, M. Meddad, O. Cherkaoui, M. Mazroui, Y. Boughaleb, L. Van Langenhove, Improvement of the electroactive β -phase nucleation and piezoelectric properties of PVDF-HFP thin films influenced by TiO2 nanoparticles, Mater. Today: Proc. 39 (2021) 1148–1152, https://doi.org/10.1016/j.matpr.2020.05.407.
[25] L. Wang, F. Gao, J. Xu, K. Zhang, J. Kong, M. Reece, H. Yan, Enhanced dielectric tunability and energy storage properties of plate-like Ba0.6Sr0.4TiO3/poly (vinylidene fluoride) composites through texture arrangement, Compos. Sci. Technol. 158 (2018) 112–120, https://doi.org/10.1016/j.compscitech.2018.02.015.
[26] Q. Zhang, F. Gao, G. Hu, C. Zhang, M. Wang, M. Qin, L. Wang, Characterization and dielectric properties of modified Ba0.6Sr0.4TiO3/poly(vinylidene fluoride) composites with high dielectric tunability, Compos. Sci. Technol. 118 (2015) 94–100, https://doi.org/10.1016/j.compscitech.2015.08.013.
[27] S. Douhi, A. Eddiai, M. Idiri, O. Cherkaoui, M. Mazroui, Investigation of SAR reduction and gain enhancement using an all-textile antenna with metamaterial structure for wireless body area network applications, Mater. Today: Proc. (2023), https://doi.org/10.1016/j.matpr.2023.12.034. S2214785323053221.
[28] I. Ibanez-Labiano, M.S. Ergoktas, C. Kocabas, A. Toomey, A. Alomainy, E. Ozden-Yenigun, Graphene-based soft wearable antennas, Appl. Mater. Today 20 (2020) 100727, https://doi.org/10.1016/j.apmt.2020.100727.
[29] S. Douhi, A. Boumegnane, N. Chakhchaoui, A. Eddiai, O. Cherkaoui, M. Mazroui, A wideband flexible antenna utilizing PMMA/PVDF-HFP/PZT polymer composite film and silver-based conductive ink for wearable applications, Polym. Adv. Tech. 35 (2024), https://doi.org/10.1002/pat.6575.
[30] S. Douhi, G.R.K. Prasad, A. Eddiai, O. Cherkaoui, M. Mazroui, S. Das, A miniaturized wearable textile UWB monopole antenna for RF energy harvesting. https://essuir.sumdu.edu.ua/handle/123456789/91112, 2023. (Accessed 25 September 2024).
[31] M.N. Hamidon, T.D. Farnana, I.H. Hasan, A. Sali, M.Md Isa, Printing of passive RFID tag antennas on flexible substrates for long read distance applications: materials and techniques, J. Sci.: Adv. Mater. Dev. 9 (2024) 100778, https://doi.org/10.1016/j.jsamd.2024.100778.
[32] A. Abdelrahman, F. Erchiqui, M. Nedil, Fabrication and evaluation of a flexible antenna device composed of a compatible iron-oxide clay in a PDMS graphene matrix, React. Chem. Eng. 9 (2024) 901–909, https://doi.org/10.1039/D2RE00352J.
[33] S. Labihi, N. Chakhchaoui, A. Eddiai, M. El Achaby, M. Meddad, O. Cherkaoui, M. Mazroui, Enhancement of piezoelectric β-polymorph formation and properties of graphene oxide and PZT-incorporated in PVDF-HFP matrix for energy harvesting applications, Polym. Compos. 44 (2023) 2296–2304, https://doi.org/10.1002/pc.27245.
[34] S. Labihi, K. Oumghar, N. Chakhchaoui, A. Eddiai, M. Meddad, O. Cherkaoui, M. El Achaby, M. Mazroui, Improvement of the piezoelectric, thermal, structural properties of PMMA/PVdF-HFP blend composite films using PZT, Eur. Phys. J. Appl. Phys. 98 (2023) 2, https://doi.org/10.1051/epjap/2022220112.
[35] B. Luo, X. Wang, Y. Wang, L. Li, Fabrication, characterization, properties and theoretical analysis of ceramic/PVDF composite flexible films with high dielectric constant and low dielectric loss, J. Mater. Chem. A 2 (2014) 510–519, https://doi.org/10.1039/c3ta14107a.
[36] M. Ma, K. Song, Y. Ji, F. Hussain, A. Khesro, M. Mao, L. Xue, P. Xu, B. Liu, Z. Lu, D. Zhou, D. Wang, S. Sun, 5G microstrip patch antenna and microwave dielectric properties of cold sintered LiWVO6–K2MoO4 composite ceramics, Ceram. Int. 47 (2021) 19241–19246, https://doi.org/10.1016/j.ceramint.2021.03.179.
[37] M.A. Darwish, A.I. Afifi, A.S. Abd El-Hameed, H.F. Abosheiasha, A.M.A. Henaish, D. Salogub, A.T. Morchenko, V.G. Kostishyn, V.A. Turchenko, A.V. Trukhanov, Can hexaferrite composites be used as a new artificial material for antenna applications? Ceram. Int. 47 (2021) 2615–2623, https://doi.org/10.1016/j.ceramint.2020.09.108.
[38] Q. Meng, X. Liu, J. Duan, Y. Zhao, B. Zhang, Ultra-wideband wearable antenna based on composite materials, J. Mater. Sci. Mater. Electron. 34 (2023) 861, https://doi.org/10.1007/s10854-023-10174-7.
[39] Z. Peng, A. Ye, L. Zhang, X. Li, C. Lian, C. Li, Micro-crosslinked polyimide nanocomposites with low dielectric constant and low dielectric loss for microwave antenna with molecular dynamics, Compos. Commun. 46 (2024) 101804, https://doi.org/10.1016/j.coco.2023.101804.
[40] C.-Y. Wei, S. Gupta, N.-H. Tai, Improving RFID performance through enhanced electromagnetic wave absorption with Fe2O3 and polytetrafluoroethylene-based bilayer polydimethylsiloxane composites, Compos. Appl. Sci. Manuf. 181 (2024) 108157, https://doi.org/10.1016/j.compositesa.2024.108157.
[41] S. Labihi, A. Eddiai, M. El Achaby, M. Rguiti, M. Mazroui, Enhancing β-phase and dielectric properties of BCZT lead-free reinforced in PVDF-HFP composite thick films for eco-friendly energy harvesting, Ceram. Int. (2024), https://doi.org/10.1016/j.ceramint.2024.07.363.
[42] H. Parangusan, D. Ponnamma, M.A.A. Al-Maadeed, Stretchable electrospun PVDF-HFP/Co-ZnO nanofibers as piezoelectric nanogenerators, Sci. Rep. 8 (2018) 754, https://doi.org/10.1038/s41598-017-19082-3.
[43] Z.L. Wang, On Maxwell's displacement current for energy and sensors: the origin of nanogenerators, Mater. Today 20 (2017) 74–82, https://doi.org/10.1016/j.mattod.2016.12.001.
[44] Z.L. Wang, On the first principle theory of nanogenerators from Maxwell's equations, Nano Energy 68 (2020) 104272, https://doi.org/10.1016/j.nanoen.2019.104272.
[45] Y. Huang, K. Boyle, Antennas: from Theory to Practice, first ed., Wiley, 2008 https://doi.org/10.1002/9780470772911.
[46] H. Jeon, S. Jin, K.-Y. Shin, Highly flexible, high-performance radio-frequency antenna based on free-standing graphene/polymer nanocomposite film, Appl. Surf. Sci. 582 (2022) 152455, https://doi.org/10.1016/j.apsusc.2022.152455.
[47] F. Xu, L. Sun, K. Zhang, L. Wang, Y. Qiu, Electromagnetic performance and impact damage of the microstrip antennas integrated in cylindrical three dimensional woven composite structures, Polym. Compos. 39 (2018) 3259–3267, https://doi.org/10.1002/pc.24338.
[48] K. Zhang, P.J. Soh, S. Yan, Design of a compact dual-band textile antenna based on metasurface, IEEE Trans. Biomed. Circuits Syst. 16 (2022) 211–221, https://doi.org/10.1109/TBCAS.2022.3151243.
[49] M. Shahpari, D.V. Thiel, Fundamental limitations for antenna radiation efficiency, IEEE Trans. Antenn. Propag. 66 (2018) 3894–3901, https://doi.org/10.1109/TAP.2018.2836447.
[50] H. Li, J. Du, X.-X. Yang, S. Gao, Low-profile all-textile multiband microstrip circular patch antenna for WBAN applications, Antennas Wirel. Propag. Lett 21 (2022) 779–783, https://doi.org/10.1109/LAWP.2022.3146435.
[51] H. Yang, X. Liu, Y. Fan, L. Xiong, Dual-band textile antenna with dual circular polarizations using polarization rotation AMC for off-body communications, IEEE Trans. Antenn. Propag. 70 (2022) 4189–4199, https://doi.org/10.1109/TAP.2021.3138504.
[52] S. Srilali, Multifunctional titanium co-doped ZnAl2O4V2O5 composite ceramic nanoparticles: enabling enhanced performance for L, S, C, and X band communications, Opt. Mater. 151 (2024) 115389, https://doi.org/10.1016/j.optmat.2024.115389.
[53] A. Rahman, H. Abdullah, M.S. Zulfakar, M.J. Singh, M.T. Islam, Microwave dielectric properties of Mn x Zn(1−x)Fe2O4 ceramics and their compatibility with patch antenna, J. Sol. Gel Sci. Technol. 77 (2016) 470–479, https://doi.org/10.1007/s10971-015-3937-4.
[54] P. Thiruramanathan, A. Marikani, S. Ravi, D. Madhavan, G.S. Hikku, Fabrication of miniaturized high bandwidth dielectric resonator on patch (DRoP) antenna using high dielectric CaCu3Ti4O12 nanoparticles, J. Alloys Compd. 747 (2018) 1033–1042, https://doi.org/10.1016/j.jallcom.2018.03.015.
[55] S. Didde, R.S. Dubey, S.K. Panda, G.S. Babu, Experimental investigation of calcium-doped zinc aluminate nanoparticles as a promising material for microwave applications, ACS Omega 8 (2023) 38064–38071, https://doi.org/10.1021/acsomega.3c03983.
[56] S. Didde, R.S. Dubey, S.K. Panda, G.S. Babu, Experimental study of doped zinc aluminate nanoparticles by bottom-up approach for microstrip patch antenna applications, J. Mater. Sci. 57 (2022) 21069–21079, https://doi.org/10.1007/s10853-022-07929-8.
[57] P. Thiruramanathan, S.K. Sharma, S. Sankar, R. Sankar Ganesh, A. Marikani, D. Y. Kim, Synthesis of bismuth titanate (BTO) nanopowder and fabrication of microstrip rectangular patch antenna, Appl. Phys. A 122 (2016) 1006, https://doi.org/10.1007/s00339-016-0549-y.